International Journal of Multiphase Flow 116 (2019) 270–280

Contents lists available at ScienceDirect

International Journal of Multiphase Flow

journal homepage: www.elsevier.com/locate/ijmulflow

A dynamic spectrally enriched subgrid-scale model for preferential concentration in particle-laden turbulence

Maxime Bassenne[a,*], Mahdi Esmaily[b], Daniel Livescu[c], Parviz Moin[a], Javier Urzay[a]

[a] Center for Turbulence Research, Stanford University, Stanford, CA 94305-3024, United States
[b] Sibley School of Mechanical and Aerospace Engineering, Cornell University, Ithaca, NY 14853, United States
[c] Los Alamos National Laboratory, Los Alamos, NM 87505, United States

ARTICLE INFO

Article history:
Received 15 November 2018
Revised 12 March 2019
Accepted 26 April 2019
Available online 26 April 2019

Keywords:
Particle-laden flows
Large-eddy simulation
Preferential concentration
Subgrid-scale modeling

ABSTRACT

A new subgrid-scale (SGS) model for turbulent velocity fluctuations is proposed for large-eddy simulations (LES) of dispersed multi-phase flows. The modeled velocity contains scales smaller than the LES grid resolution, thereby enabling the prediction of small-scale phenomena such as the preferential concentration of particles in high-strain regions. The construction of the spectrally enriched velocity field in physical space is made dynamically, and is based on (1) modeling the smallest resolved eddies of sizes comparable to the LES grid size via approximate deconvolution, and (2) reconstructing the SGS fluctuations via non-linear generation of small-scale turbulence. The model does not contain tunable parameters, can be deployed in non-uniform grids, and is applicable to inhomogeneous flows subject to arbitrary boundary conditions. The performance of the model is assessed in LES of isotropic turbulence laden with inertial particles, where improved agreement with direct numerical simulation results is obtained for the statistics of preferential concentration.

1. Introduction

Particle-laden turbulence is ubiquitous in engineering and environmental flows. A particular feature of these types of flows is the presence of particle clouds that result from the tendency of inertial particles to preferentially sample specific regions of the turbulent flow field (Lazaro and Lasheras, 1989; Balachandar and Eaton, 2012; Monchaux et al., 2010; 2012; Esmaily-Moghadam and Mani, 2016; Baker et al., 2017). The intensity and spectral properties of these clouds are central to a number of physical processes. These include momentum and thermal inter-phase coupling with the turbulent environment (Ferrante and Elghobashi, 2003; Frankel et al., 2016; Richter et al., 2016; Pouransari and Mani, 2017; 2018; Horwitz and Mani, 2018; Balachandar et al., 2019), dispersion due to electric forces (Renzo and Urzay, 2018; Yao and Capecelatro, 2018), and thermal coupling with an external radiative heat source (Rahmani et al., 2015; Villafañe et al., 2017; Jofre et al., 2017). It is therefore of relevance in computational predictions of these phenomena to resolve or model the characteristic scales associated with the resulting inhomogeneities in the spatial distribution of particles caused by these clouds.

The cost of resolving all flow length scales down to the Kolmogorov scales via Direct Numerical Simulations (DNS) often becomes prohibitive for industrial- and environmental-scaled systems. An alternative approach consists of employing LES by integrating the low-pass-filtered Navier–Stokes equations

$$\frac{\partial \overline{u}_i}{\partial x_i} = 0, \tag{1}$$

$$\frac{\partial \overline{u}_i}{\partial t} + \overline{u}_j \frac{\partial \overline{u}_i}{\partial x_j} = -\frac{1}{\rho}\frac{\partial \overline{p}}{\partial x_i} + \nu \frac{\partial^2 \overline{u}_i}{\partial x_j \partial x_j} - \frac{\partial \tau_{ij}}{\partial x_j}, \tag{2}$$

where the overlined quantities $\overline{(\cdot)}$ correspond to large-scale portions of the corresponding fields. In this formulation, t is the time coordinate, x_i are spatial coordinates, u_i are flow velocity components, p is the hydrodynamic pressure, ρ is the density, and ν is the kinematic viscosity. The symbol $\tau_{ij} = \overline{u_i u_j} - \overline{u}_i \overline{u}_j$ denotes the unclosed SGS stress tensor, which, in this study, is closed using traditional models for single-phase flows. More importantly, and since the particles are transported by the equation of motion

$$\frac{du_{p,i}}{dt} = \frac{u_i - u_{p,i}}{t_a}, \tag{3}$$

is to consider a closure for the full-scale flow velocity u_i to which the particles are subjected. In the notation, $x_{p,i}$ is the position of the particle, $u_{p,i}$ is its velocity, and $t_a = (2/9)(\rho_p/\rho)(a^2/\nu)$ is the

* Corresponding author.
E-mail address: bassenne@stanford.edu (M. Bassenne).

https://doi.org/10.1016/j.ijmultiphaseflow.2019.04.025
0301-9322/

characteristic acceleration time, with ρ_p and a the particle density and radius, respectively. In writing Eq. (3), it is has been assumed that the particle radius is much smaller than the Kolmogorov length scale, that the particle density is much larger than that of the carrier fluid, and that the particle Reynolds number computed using the slip velocity as characteristic velocity is much smaller than unity (Maxey and Riley, 1983).

An accurate time integration of Eq. (3) requires the full-scale carrier-phase velocity u_i rather than the filtered one $\overline{u}_i$. Inaccurate predictions of some of the dispersed-phase statistics are typically observed when this closure problem is ignored and $\overline{u}_i$ only is employed for the integration of Eq. (3), or equivalently, when the equation

$$\frac{du_{p,i}}{dt} = \frac{\overline{u}_i - u_{p,i}}{t_a} \tag{4}$$

is solved instead of Eq. (3) (Marchioli, 2017; Chen and Jin, 2017). The magnitude of the inaccuracies made in the predictions is however dependent on the characteristic dimensionless parameters of the problem, and most notably, on the SGS Stokes number St_{SGS}, which represents the ratio of the characteristic particle acceleration time to the turnover time of the eddies whose size is equal to the grid size, as described in Urzay et al. (2014). Among the dispersed-phase statistics degraded by neglecting the closure problem described above [i.e., by integrating Eq. (4) in place of Eq. (3)] is preferential concentration, whose intensity and associated scales have been shown to be inaccurately predicted (Park et al., 2017; 2015).

Most studied SGS models consist of approximate-deconvolution or Lagrangian stochastic models (Minier, 2015; Mazzitelli et al., 2014; Marchioli, 2017; Shotorban and Mashayek, 2006; Johnson and Meneveau, 2018; Rani et al., 2014; Pozorski and Apte, 2009), or a combination of the two (Michalek et al., 2013). A class of less investigated SGS models are the spectrally enriched ones, which are typically based on kinematic simulation (Ray and Collins, 2014; Murray et al., 2016; Zhou et al., 2018; Pozorski and Rosa, 2019), fractal interpolation (Marchioli et al., 2008a; 2008b; Akinlabi et al., 2018) or spectrally-optimized interpolation (Gobert and Manhart, 2011). The main drawbacks associated with this class of models are their reliance on Fourier basis functions with infinite support in physical space, and on tunable parameters whose values outside of the homogeneous turbulence regime are not straightforward to justify theoretically. In addition, it is challenging to generate small-scale turbulence structures that display the correct degree of spatiotemporal correlations (Jiménez et al., 1993; Bürger et al., 2013; He et al., 2017; Ghate and Lele, 2017), and to which the particles are sensitive during their flight and accumulation into clouds. The model presented in this paper circumvents some of these limitations.

In this paper, an SGS model, termed spectrally enriched differential filter model (SDF), is proposed that is formulated in physical space for the full-scale carrier-phase velocity u_i to be used in the integration of the equation of particle motion (3) in LES of particle-laden turbulence. This investigation builds on some of our previous work (Urzay et al., 2014; Park et al., 2017; 2015; Bassenne et al., 2015; 2017b; 2017a; 2018b) by proposing a SGS model based on differential filters that incorporates a spectrally-enriched carrier-phase velocity u_i, which contains scales smaller than the LES grid resolution, thereby enabling the calculation of small-scale phenomena such as preferential concentration of particles. The model is dynamic, in that it does not contain tunable parameters, it can be deployed in non-uniform grids, and is applicable to inhomogeneous flows subject to arbitrary boundary conditions (Bassenne et al., 2018a).

The remainder of this paper is organized as follows. The SGS model formulation is described in Section 2. Results for the carrier- and dispersed-phase statistics obtained from LES with and without the SGS model, and their comparisons with DNS, are provided in Section 3. Lastly, concluding remarks and suggestions for future work are provided in Section 4.

2. Description of the SDF model

This section describes the SDF model proposed in the present work. Consider the velocity field $u_i^{(2\Delta)}$ described by its nodal values on a grid with characteristic spacing 2Δ. This velocity and this grid resolution are equivalent, respectively, to the LES velocity field $\overline{u}_i$ and to the LES grid resolution. Using these quantities, Fig. 1 shows the three-step (I, II, III) SDF model algorithm employed to regenerate the velocity field on a finer grid.

The first step of the SDF model algorithm (step I in Fig. 1) makes use of the dynamic approximate-deconvolution differential filter (DF) model developed in Park et al. (2017, 2015) and leads to a velocity field $u_{i,\mathrm{AD}}^{(2\Delta)}$ still defined on the original grid. Section 2.1 is devoted to explaining this procedure.

The second step (II in Fig. 1) of the SDF model is described in Section 2.2 and is composed of the following substages: (i) interpolation, which leads to a velocity field $u_{i,\mathrm{ADI}}^{(\Delta)}$ defined on the finer grid, (ii) spectral enrichment, which provides a velocity field $u_{i,\mathrm{SGS}}^{(\Delta)}$ furnished with fine scales, and (iii) approximate deconvolution, which renders a velocity field $u_{i,\mathrm{AD}}^{(\Delta)}$ also defined on the finer grid but energized near the cutoff. These three substages are applied once for a single-level reconstruction that corresponds to refining the grid by a factor of two in each direction. This second step can be applied recursively to obtain higher levels of refinement, as depicted in Fig. 1.

Lastly, since the velocity field $u_{i,\mathrm{AD}}^{(\Delta)}$ is generally not divergence-free, the final step of the SGS model algorithm (step III in Fig. 1) consists of extracting the solenoidal portion of $u_{i,\mathrm{AD}}^{(\Delta)}$, which results in the full-scale modeled velocity field u_i employed for integrating the equation of motion of the particles (3).

2.1. Step I: dynamic approximate deconvolution

Given $u_i^{(2\Delta)}$, an approximately-deconvolved velocity field $u_{i,\mathrm{AD}}^{(2\Delta)}$ is computed in the following way. To benefit from a filtering kernel that is easily applicable to complex geometries, the dynamic differential-filter approximate-deconvolution model in Park et al. (2017, 2015) is used in the present study, which provides the expression

$$u_{i,\mathrm{AD}}^{(2\Delta)} = u_i^{(2\Delta)} - \frac{\partial}{\partial x_j}\left\{[b^{(2\Delta)}]^2 \frac{\partial u_i^{(2\Delta)}}{\partial x_j}\right\}. \tag{5}$$

The parameter $b^{(2\Delta)}$ scales with the local filter-width size and is dynamically computed by solving a simple quadratic equation using the procedure based on SGS kinetic-energy matching described in Park et al. (2017, 2015). The parameter $b^{(2\Delta)}$ is non-uniform in space along non-homogeneous coordinates. When $b^{(2\Delta)}$ is uniform, as in the present study, the deconvolved velocity $u_{i,\mathrm{AD}}^{(2\Delta)}$ is divergence-free. In comparison with the input velocity $u_i^{(2\Delta)}$, the spectral kinetic energy of $u_{i,\mathrm{AD}}^{(2\Delta)}$ near the grid cutoff wavenumber is enhanced, yet the resulting flow does not contain scales smaller than the grid cutoff.

2.2. Step II: interpolation, spectral enrichment, and approximate deconvolution

The SDF model supplements the approximately-deconvolved velocity $u_{i,\mathrm{AD}}^{(2\Delta)}$ with subgrid scales as follows. The velocity field

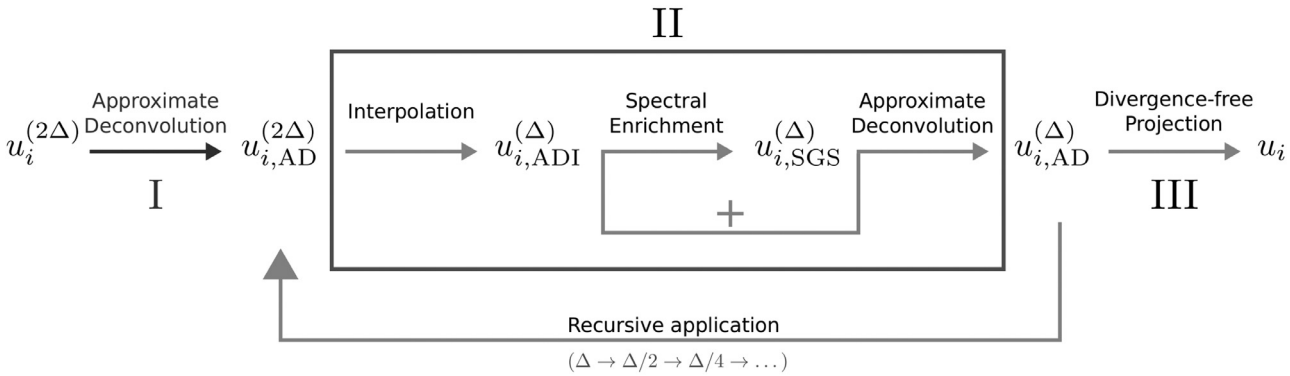

Fig. 1. Schematic diagram of the steps I, II, and III involved in the SDF model algorithm. The diagram assumes an input LES velocity $\overline{u}_i = u_i^{(2\Delta)}$ represented on a grid with characteristic resolution 2Δ, and provides a full-scale modeled velocity u_i defined on a finer grid.

$u_{i,\mathrm{ADI}}^{(\Delta)}$ is obtained by interpolating $u_{i,\mathrm{AD}}^{(2\Delta)}$ onto the finer grid. This interpolation step does not lead to small scales that have any significant energy. However, it raises numerical challenges that are worth discussing. In particular, the interpolating kernels generally lead to artificial smoothing of the resolved velocity fluctuations that hinder the conservation of kinetic energy. The latter is nonetheless a quantity that plays a critical role in subsequent steps of the dynamic modeling approach outlined below. This issue is more severe in three-dimensional staggered grids where a refinement by a factor of two in each direction implies that none of the face centers of the original grid coincide with the face centers of the fine one. In this study, this issue is mitigated by using fourth-order Lagrange interpolation onto a collocated mesh in order to minimize the shift in variable location carried along in a staggered mesh. Note however that the full-scale modeled velocity u_i is requested on a staggered grid to facilitate the divergence-free projection. As a result, the velocity is interpolated onto a staggered grid only during the final refinement level.

The interpolated velocity $u_{i,\mathrm{ADI}}^{(\Delta)}$ has scales ranging from the integral scale to the LES cutoff 2Δ, and does not contain any significant SGS motion in scales smaller than that. In contrast, the energy of the spectrally enriched velocity $u_{i,\mathrm{SGS}}^{(\Delta)}$ is mostly populated in the subgrid scales ranging from Δ to 2Δ. As a consequence, $u_{i,\mathrm{SGS}}^{(\Delta)}$ bears the regenerated scales by spectral enrichment and requires modeling. In this study, the proposed model for $u_{i,\mathrm{SGS}}^{(\Delta)}$ is

$$u_{i,\mathrm{SGS}}^{(\Delta)} = \sqrt{2K}\frac{D_i}{\sqrt{D_j D_j}}. \tag{6}$$

Expression (6) is composed of two multiplicative terms that involve the square root of the local SGS kinetic energy $K = u_{i,\mathrm{SGS}}^{(\Delta)} u_{i,\mathrm{SGS}}^{(\Delta)}/2$ based on the SGS velocity, and the normalized vector $D_i/\sqrt{D_j D_j}$ that describes the relative magnitude of each velocity component, with D_i being an estimate of the local instantaneous growth-rate vector. The computation of K and D_i is explained below.

The growth-rate vector of the SGS motion is modeled as

$$D_i = N_i - \widetilde{N}_i, \tag{7}$$

where N_i is given by

$$N_i = \left[u_{j,\mathrm{ADI}}^{(\Delta)} - \widetilde{u_{j,\mathrm{ADI}}^{(\Delta)}}\right]\frac{\partial u_{i,\mathrm{ADI}}^{(\Delta)}}{\partial x_j}, \tag{8}$$

and $\widetilde{(\cdot)}$ denotes a spatial filter with characteristic width 4Δ (i.e., twice as coarse as the LES grid). In Eq. (7), $\widetilde{N}_i$ is subtracted from N_i to minimize the modification of the resolved portion of N_i. The model form for the SGS velocity $u_{i,\mathrm{SGS}}^{(\Delta)}$ obtained by combining Eqs. (6)-(8) resembles the physical mechanism of generation of small scales by convection of large scales in turbulent flows. However, it models neither the pressure and viscosity effects on the generation or suppression of small scales, nor the temporal dynamics inherent to the generation process. Instead, the present model assumes that the subgrid scales are instantaneously generated by one round of interactions among the resolved scales. Although the model is similar to the velocity-estimation model for the SGS stress tensor in Domaradzki and Loh (1999), the present work reformulates it in the form given by Eq. (6), employs a dynamic approximate-deconvolution scheme, and also provides a dynamic procedure for the computation of the prefactor $\sqrt{2K}$, as described below.

The local SGS kinetic energy $K = u_{i,\mathrm{SGS}}^{(\Delta)} u_{i,\mathrm{SGS}}^{(\Delta)}/2$ is estimated assuming that it is proportional to the kinetic energy of the smallest resolved scales. This assumption resembles local self-similarity and leads to

$$K = K_{1,2} = \mathcal{C} K_{2,4}, \tag{9}$$

where $\mathcal{C}$ is a proportionality coefficient that is dynamically computed as

$$\mathcal{C} = \langle K_{2,4}\rangle / \langle K_{4,8}\rangle. \tag{10}$$

In Eq. (10), the angle brackets denote averaging along homogeneous directions. If the latter are not present in a particular flow configuration, the angle brackets are substituted by a series of filtering operations to regularize the dynamic coefficient, as traditionally performed in LES dynamic procedures. In the above formulation, $K_{m,n}$ denotes the kinetic energy of eddies whose sizes range from $m\Delta$ to $n\Delta$, namely

$$K_{2,4} = \left(u_{i,\mathrm{ADI}}^{(\Delta)} - \widehat{u_{i,\mathrm{ADI}}^{(\Delta)}}\right)\left(u_{i,\mathrm{ADI}}^{(\Delta)} - \widehat{u_{i,\mathrm{ADI}}^{(\Delta)}}\right)/2 \tag{11}$$

and

$$K_{4,8} = \left(\widehat{u_{i,\mathrm{ADI}}^{(\Delta)}} - \widehat{u_{i,\mathrm{ADI}}^{(\Delta)}}\right)\left(\widehat{u_{i,\mathrm{ADI}}^{(\Delta)}} - \widehat{u_{i,\mathrm{ADI}}^{(\Delta)}}\right)/2, \tag{12}$$

where $\widehat{(\cdot)}$ denotes a spatial filter with characteristic width 8Δ.

The motivation for the above dynamic procedure is best explained by making use of a power-like law for the kinetic-energy spectrum, $E_k(\kappa) \sim \kappa^{-\beta}$, where κ is the wavenumber and β is an exponent. It directly follows from this assumption that the ratio $K_{m,2m}/K_{2m,4m}$ is equal to a constant $\mathcal{C}$ independent of m. Additionally, under the assumption of spectrally-sharp cutoff filters for the operators $\widehat{(\cdot)}$ and $\widetilde{(\cdot)}$ in Eqs. (11) and (12), the ratio $K_{m,2m}/K_{2m,4m} = 2^{1-\beta}$ is obtained. Note that β can be imposed, for instance, using Kolmogorov's scaling $\beta = 5/3$, thereby leading to a theoretical value of the parameter constant $\mathcal{C} = 0.63$. Instead, the present model does not explicitly require any value of β since the formulation uses a dynamic computation of $\mathcal{C}$ based on cascade energetics of the resolved scales, as in Eq. (10).

The scale-similarity assumption implied by Eq. (9) regarding the ratio of kinetic energies being independent of the specific wavenumber band becomes increasingly more unjustified near and within the viscous range, where the kinetic-energy spectrum no longer varies as a power law but rather does so exponentially. The higher the Reynolds number, the longer the inertial range is and the larger the number of reconstruction steps are that can be performed with the SDF model without deleterious incursions into the unmodeled viscous subrange. Similarly, the scale-similarity assumption may become unjustified at the first reconstruction level unless the Reynolds number is sufficiently large and the grid cutoff of the base LES is far away from the integral scales. This can be understood by noticing that the first reconstruction level requires information of the kinetic energy up to scales four times larger than the grid cutoff of the base LES.

After the spectral enrichment, the final substage of step II consists of approximately deconvolving the sum of the interpolated velocity field $u_{i,\mathrm{ADI}}^{(\Delta)}$ and spectrally enriched fluctuation velocity $u_{i,\mathrm{SGS}}^{(\Delta)}$ using the differential filter

$$u_{i,\mathrm{AD}}^{(\Delta)} = \left(u_{i,\mathrm{ADI}}^{(\Delta)} + u_{i,\mathrm{SGS}}^{(\Delta)}\right) - \frac{\partial}{\partial x_j}\left\{\left[b^{(\Delta)}\right]^2 \frac{\partial}{\partial x_j}\left(u_{i,\mathrm{ADI}}^{(\Delta)} + u_{i,\mathrm{SGS}}^{(\Delta)}\right)\right\}. \quad (13)$$

In Eq. (13), $b^{(\Delta)}$ is chosen such that $b^{(\Delta)} = b^{(2\Delta)}/2$ in order to account for the doubled grid resolution, and to keep constant the deconvolution filter width relative to the grid resolution [i.e., $b^{(\Delta)}/\Delta = b^{(2\Delta)}/(2\Delta)$]. This substep is intended to correct for the numerical errors caused at high wavenumbers by the discrete operators employed in the spectral-enrichment step.

As depicted in Fig. 1, the aforementioned three substages (i.e., interpolation, spectral enrichment, and approximate deconvolution) can be applied recursively for successive refinement levels, leading to increasingly finer-scale velocity fields.

2.3. Step III: divergence-free projection

After recursive application of step II, the final output velocity $u_{i,\mathrm{AD}}^{(\Delta)}$ is forced to be divergence-free using a classic Hemholtz decomposition. In this way, a Poisson equation

$$\frac{\partial \phi}{\partial x_j \partial x_j} = \frac{\partial u_{i,\mathrm{AD}}^{(\Delta)}}{\partial x_i} \quad (14)$$

is solved for the potential ϕ of the irrotational portion of the velocity field $u_{i,\mathrm{AD}}^{(\Delta)}$. The solenoidal portion of $u_{i,\mathrm{AD}}^{(\Delta)}$ is therefore given by

$$u_i = u_{i,\mathrm{AD}}^{(\Delta)} - \frac{\partial \phi}{\partial x_i}. \quad (15)$$

The resulting incompressible velocity field u_i is used as a model for the full-scale flow velocity in integrating the equation of motion of the particles (3). Generally, the computational cost of the model is mostly limited by this step, particularly when the flow configuration does not have periodic directions, since it requires the resolution of a linear system of equations on a grid finer than the original LES grid.

2.4. Pathways for further improvement of the SDF model

Three aspects are worth pointing out with regard to the formulation described above. They pertain to possible shortfalls of the model that could motivate future work.

In the SDF model, the motion of the small scales is generated at each reconstruction level. By doing so, however, the motion of the large scales is modified as well. This is expected from the physical-space formulation of the SDF model, which relies on spectrally non-compact numerical operators. Note that this lack of spectral compactness contributes to generate variations in the dynamic coefficient C as the grid is refined.

The subgrid scales regenerated by the SDF model above are temporally correlated in time with the same correlation time as the fluctuations corresponding to the near-cutoff eddies. This is not a realistic assumption, in that the small scales should decorrelate faster, and it may have consequences on the persistence time of the particle clouds that should be interrogated in future work.

The description of the SDF model provided above (see schematics in Fig. 1) can be modified if significant computational cost savings are pursued. In its present form, the cost of the SDF model is of the same order as the cost of a traditional LES simulation (i.e., without SGS model for the velocity) at the refined grid corresponding to the particular reconstruction level. For instance, one potential path for improving the computational cost consists of non-uniformly deploying the SDF model in space, in a way that the number of refinement levels employed in the algorithm would be allowed to vary spatially and would be dynamically computed. Similarly, the computational overhead could be greatly decreased by spectral enrichment formulations that would analytically incorporate the divergence-free condition on the modeled field, rather than enforcing it through the inversion of Eq. (14). Existing noise-reducing linear filters or approximate Poisson solvers replacing the traditional resolution of Eq. (14) would also be of interest for accelerating the step III in the present algorithm (Schiavazzi et al., 2014). These computational aspects are worthy of future research.

3. Model performance

In this section, results obtained from the application of the SDF model to one-way coupled, homogeneous-isotropic particle-laden turbulence are described. The focus of the analysis is on the impact of the SDF model on preferential-concentration statistics in regimes where the small-scale eddies play a critical role in predicting the accurate spatial distribution of particles.

3.1. Computational set-up

The DNS reference simulations employed in the analysis are obtained by solving the Navier–Stokes equations in a triply-periodic cubic domain using a finite-volume solver that employs second-order accurate in space and fourth-order accurate in time numerics, as described in Esmaily-Moghadam and Mani (2016) and Esmaily et al. (2018). The constant-energy linear forcing proposed in Bassenne et al. (2016) is used in the momentum equation in order to sustain the turbulence and achieve statistical stationarity. The Reynolds number based on the Taylor microscale is $\mathrm{Re}_\lambda = 85$. The DNS employs 256^3 grid points that are equivalent to a grid resolution $\kappa_{\max}\ell_k = 1.6$, with $\kappa_{\max} = \pi/\Delta$ being the largest wavenumber resolved by the grid. The Kolmogorov length is $\ell_k = (\nu^3/\epsilon)^{1/4}$, where ν is the kinematic viscosity and ϵ is the mean molecular dissipation. The integral length is equal to $\ell = u_\ell^3/\epsilon$ where u_ℓ is the root mean square large-scale velocity $u_\ell = \sqrt{u_i u_i/3}$.

The analysis includes comparisons of DNS with LES obtained by solving the filtered Navier–Stokes Eqs. (1) and (2). The SGS stress tensor is modeled in LES using the dynamic Smagorinsky model (Germano et al., 1991), where the dynamic coefficient is calculated using the least-squares approach of Lilly (1992). The LES employs 32^3 grid points with a grid resolution $\kappa_{\max}\ell_k = 0.2$. In order to account for the unresolved portion of the kinetic energy that is not captured in LES, the value of the resolved kinetic energy injected in LES is set to 85% of the corresponding DNS kinetic energy. This resolved kinetic energy is obtained by filtering the DNS with a box filter that has a filter width equal to the LES grid spacing. All spatial filters are chosen to be box filters numerically implemented with a fourth-order Simpson rule for quadrature.

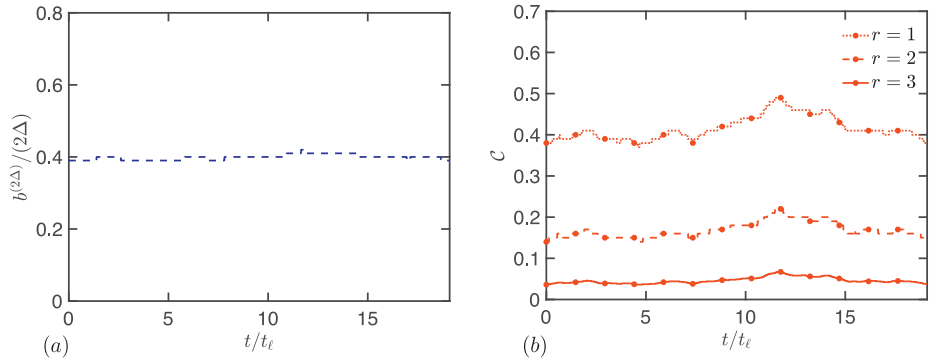

Fig. 2. Time history of the spatially-uniform dynamic coefficients (a) b and (b) $\mathcal{C}$ of the SDF model at different levels of refinement r, where the grid is refined by a factor 2^r in each direction relative to the LES grid.

A large number of particles $N_p = 5 \times 256^3$ are randomly seeded once the motion of the carrier phase has reached a statistically steady state. The value of N_p is chosen to enable a physically meaningful interpretation of the number-density spectra arising from the computation of the Eulerian number-density field based on a nearest-neighbor counting method, as discussed in Bassenne et al. (2017b). Data collection starts after a time sufficiently long compared to the characteristic particle acceleration time and to the time required for preferential-concentration statistics to become stationary (Jin et al., 2010). Specifically, time-averaged statistics are computed from 19 snapshots recorded during $13t_\ell$, with $t_\ell = \ell/u_\ell$ the integral time calculated using the associated integral length ℓ and fluctuation velocity u_ℓ. All Eulerian flow velocity fields appearing in the particle equations of motion are interpolated to the particle position using second-order Lagrange interpolation.

At every substep of the time-advancement scheme, the full-scale velocity u_i in Eq. (3) is set equal to (a) the DNS velocity (denoted as DNS in the set of results presented below), (b) the resolved velocity $\overline{u}_i$ without any SGS model (denoted as LES), (c) the resolved velocity $\overline{u}_i$ supplemented with a differential-filter approximate-deconvolution-modeled turbulent fluctuation velocity on the LES grid as described in Park et al. (2017, 2015) (denoted as LES-DF), and (d) the full-scale modeled velocity obtained from the SDF model as described in Section 2.2. In the latter, the levels of reconstruction are varied from a single one (LES-SDF 1), to two (LES-SDF 2) and three (LES-SDF 3), which correspond to recovering a velocity field on grids with 64^3, 128^3 or 256^3 cells, respectively. Therefore, the third reconstruction level (LES-SDF 3) leads to a full-scale modeled velocity field that is defined on the same grid as the DNS.

The relevant dimensionless parameter to consider is the Stokes number

$$\mathrm{St}_k = t_a/t_k, \tag{16}$$

with $t_k = \ell_k^2/\nu$ the Kolmogorov turnover time. The results presented below correspond to values of St_k ranging from 1/4 to 8. Note that the time step utilized in these simulations is $\Delta t = 0.03t_k$ in all cases, which, in the most stringent case $\mathrm{St}_k = 1/4$, represents a time step of $\Delta t = 0.12t_a$ relative to the characteristic particle acceleration time.

3.2. Carrier-phase statistics

In the type of flows studied here, the dynamic procedures described in Section 2 yield uniform and statistically steady values for the model parameters b and $\mathcal{C}$. Their time histories are reported in Fig. 2 for illustration. The parameter b shown in Fig. 2(a) is equal to 0.40 in average, which is consistent with the value reported in Park et al. (2017, 2015). This resulting mean value of b corresponds to a differential filter that has the same second moment as a spherical top-hat filter of radius 1.3 times the LES grid resolution, thereby suggesting that the dynamic procedure yields a realistic value of the effective filter width. Similarly, the predicted time-averaged values of the dynamic coefficient $\mathcal{C}$ shown in Fig. 2(b) are 0.42, 0.17 and 0.046 for the first, second and third levels of reconstruction, respectively. Note that, as the number of reconstruction levels increases, $\mathcal{C}$ deviates from the theoretical value 0.63 estimated from the Kolmogorov scaling. This departure occurs because the dynamic procedure becomes increasingly biased by modeling and numerical errors as the reconstruction level increases, because the filters involved in computing (11) and (12) are not spectrally sharp, and because the wavenumber extent of the inertial subrange is rather limited in these simulations.

It is instructive to analyze the qualitative properties of the velocity field u_i obtained from the SDF model in comparison to the original LES velocity field $\overline{u}_i$. For instance, the instantaneous cross sections of the velocity component u_1 are shown in Fig. 3, where the DNS contours contain small-scale features that are absent in the much coarser baseline LES contours. The earlier differential-filter approximate deconvolution model leads to amplification of the fluctuations at small resolved scales on the LES grid, with the large scales remaining mostly unchanged. The lack of spectral enrichment in the differential-filter approximate-deconvolution model results in contours of u_1 that do not encompass flow structures smaller than those already observed in the LES. This feature has been reported earlier as the main intrinsic limitation of the model in Park et al. (2017, 2015), and it also pervades non-spectrally enriched SGS models at large. In contrast, the contours obtained from the SDF model incorporate smaller-scale turbulent fluctuations, as shown in Fig. 3(d-f). These fluctuations are deployed by the SDF model in a way that correlates well with locations of non-zero velocity gradients in the unmodeled LES field, in accord with Eqs. (8) and (9). Although the dynamic coefficients are spatially uniform, the kinetic energy locally injected in the subgrid-scales is proportional to the local kinetic energy at larger scales, as shown in Eq. (9). As the number of reconstruction levels increases from one to three, the modeled velocity becomes increasingly more populated at high wavenumbers.

The qualitative observations made above are similarly quantified in the spectra of kinetic energy and enstrophy of the carrier phase, which are shown in Fig. 4. While all spectra coincide at low wavenumbers, substantial differences are observed at intermediate scales near the LES grid cutoff and in the subgrid scales. In particular, the SDF model increasingly regenerates the spectral energy beyond the cutoff wavenumber with increasing number of reconstruction levels. Nonetheless, spurious oscillations are observed in the resulting spectra at evenly spaced wavenumbers.

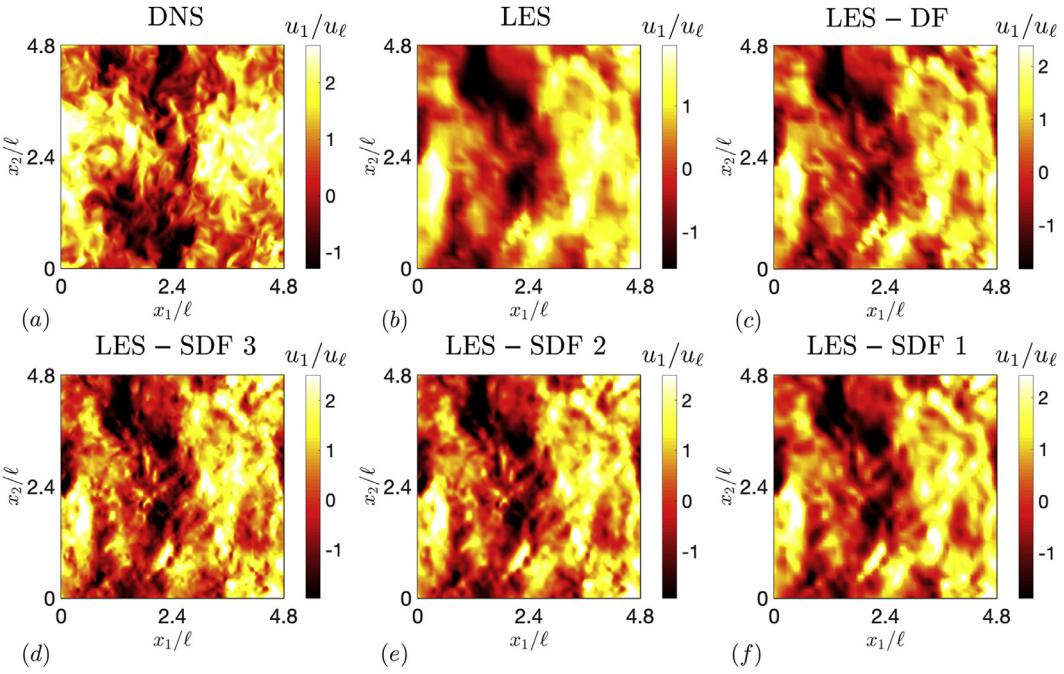

Fig. 3. Instantaneous mid-plane cross sections of the x_1 component of the carrier-phase velocity normalized with the characteristic large-scale velocity u_ℓ in the DNS case. The panel includes (a) DNS on a 256^3 grid and (b) LES on a 32^3 grid. The rest of the panels include the modeled x_1 component of the carrier-phase velocity for (c) the differential-filter approximate-deconvolution model in Park et al. (2017, 2015) on a 32^3 grid, and (d-f) the SDF model on a $(2^r \times 32)^3$ grid corresponding to the reconstruction levels $r = 1, 2, 3$. The extrema of the color maps are chosen to represent the 2.5% and 97.5% percentiles of the velocity contours.

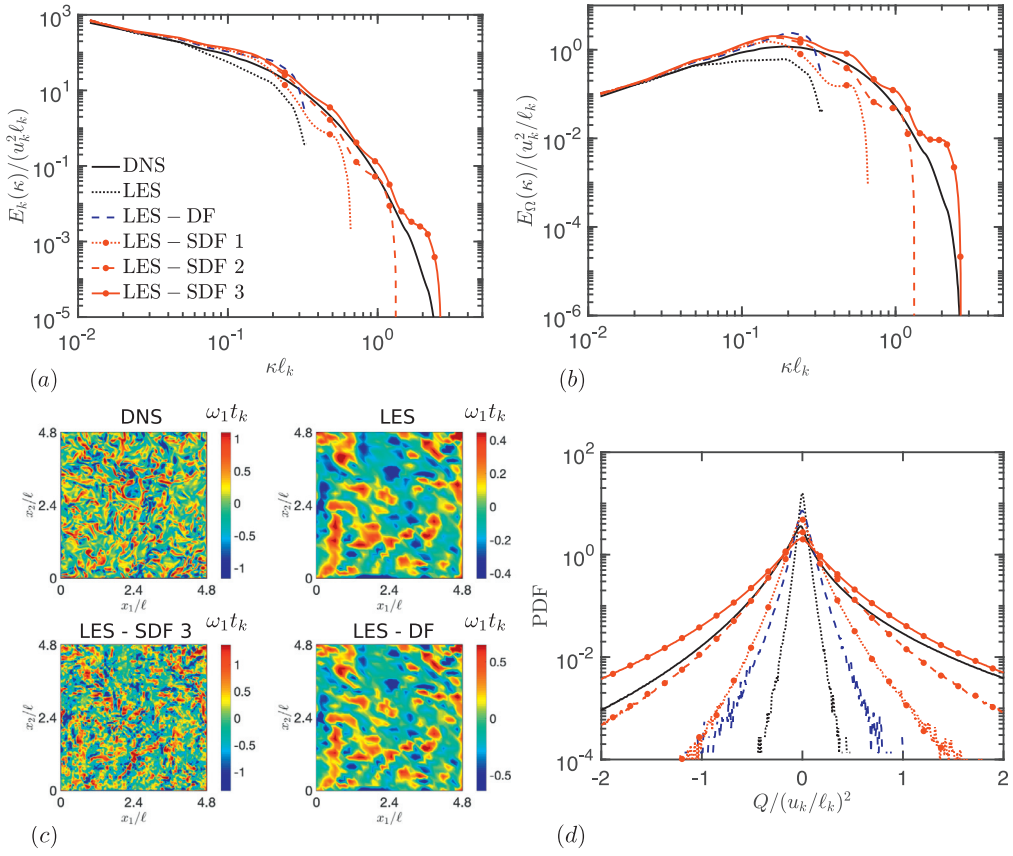

Fig. 4. Carrier-phase ensemble-averaged Fourier spectra of (a) kinetic energy and (b) enstrophy. The figure also includes (c) instantaneous mid-plane cross sections of the x_1 component of the carrier-phase vorticity normalized with $1/t_k$ for the DNS, LES, LES-DF and LES-SDF 3 cases. The extrema of the color maps are chosen to represent the 2.5% and 97.5% percentiles of the vorticity contours. (d) shows ensemble-averaged PDF of the second invariant of the velocity gradient tensor Q. In panels (a), (b), and (d), the different curves correspond to DNS (256^3), LES (32^3), LES-DF (32^3), LES-SDF 1 (64^3), LES-SDF 2 (128^3) and LES-SDF 3 (256^3) [see legend in panel (a) for line types].

These oscillations are caused by numerical errors made in step II of the SDF model algorithm and are related to the recursive dyadic-based reconstruction of the velocity. This phenomenon can be best understood by considering a hypothetical simpler choice of the interpolating kernel such as a second-order Lagrange interpolation. With that choice, since the interpolant is linear, the Laplacian of the interpolated field $u^{(\Delta)}_{i,\mathrm{ADI}}$ would be zero at grid points on the fine grid that are not present on the original coarse grid. If, additionally, the spectral enrichment would produce a zero-valued dynamic coefficient $\mathcal{C}$, the Laplacian of $u^{(\Delta)}_{i,\mathrm{SGS}}$ would also be zero at those points. As a result, the final substage of approximate deconvolution in step II would generate a zero fluctuating velocity only in that subset of points, which would be evenly spaced in the case of a Cartesian grid, and which would result in spurious oscillations in the spectra at evenly spaced wavenumbers. In the current computational set-up, however, the SDF model implementation uses fourth-order Lagrange interpolation instead of second-order, although it also generates small values of the velocity Laplacian at the aforementioned points. Similarly, the dynamic coefficient $\mathcal{C}$ is not strictly zero, but it approaches increasingly smaller values as the reconstruction level is increased.

One relevant carrier-phase statistics to analyze in relation to preferential concentration pertains to the velocity gradients. The vortex centrifugation mechanism is consensually accepted for particles at small Stokes numbers (Balachandar and Eaton, 2012). Specifically, the particles accumulate preferentially in interstitial zones where the strain rate is large after being centrifuged from the intense small vortices, in accordance with previous analyses (Maxey, 1987; Squires and Eaton, 1991; Wang and Maxey, 1993). The instantaneous cross sections of the carrier-phase vorticity component $\omega_1 = \partial u_3/\partial x_2 - \partial u_2/\partial x_3$ are shown in Fig. 4(c). In particular, both DNS and LES-SDF contours contain a large number of fine-grained vortical features that are absent in the much coarser LES, including the simulations with the differential-filter approximate-deconvolution model in Park et al. (2017, 2015). Despite the relevance of the vorticity, note that a number of authors have proposed alternative explanations for the clustering of particles at large Stokes numbers, including the sweep-stick mechanism described in Chen et al. (2006), Goto and Vassilicos (2006), Goto and Vassilicos (2008), Coleman and Vassilicos (2009) and Bragg et al. (2015), in which particles are assumed to stick to zero-acceleration fluid points that are observed to cluster in turbulent flows. The assessment of the sweep-stick mechanism within the context of the present modeling strategy is a subject worthy of future work.

The enhanced range of scales obtained by the SDF model is also illustrated by the PDF of the second invariant of the velocity-gradient tensor $Q = (1/2)(\Omega_{ij}\Omega_{ij} - S_{ij}S_{ij})$ shown in Fig. 4(d), where Ω_{ij} and S_{ij} are the rotation and strain-rate tensors, respectively. The prediction of the statistics of Q is particularly relevant for the purposes of this study, since, in preferentially-concentrated regimes, particles tend to accumulate in straining regions (i.e., $Q<0$) and are centrifuged away from vortical regions (i.e., $Q>0$) (Robinson, 1956; Maxey, 1987). However, as observed in Fig. 4(c), the baseline LES tends to heavily underpredict vortical intermittency, and as a result, leads to exceedingly narrow PDFs of Q when compared to DNS, as shown in Fig. 4(d). The utilization of the differential-filter approximate-deconvolution model in Park et al. (2017, 2015) partially palliates this problem. In contrast, improved

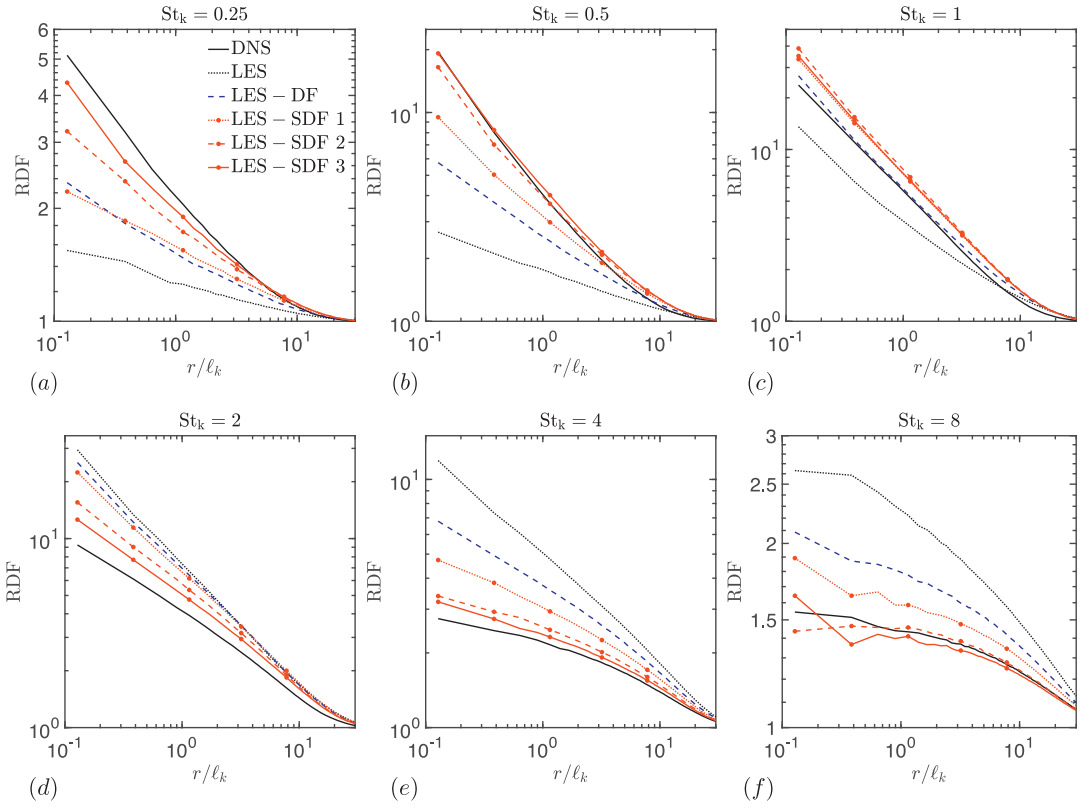

Fig. 5. Ensemble-averaged radial distribution functions (RDFs) for (a) $\mathrm{St_k} = 0.25$, (b) $\mathrm{St_k} = 0.5$, (c) $\mathrm{St_k} = 1$, (d) $\mathrm{St_k} = 2$, (e) $\mathrm{St_k} = 4$, and (f) $\mathrm{St_k} = 8$. The different curves correspond to DNS (256^3), LES (32^3), LES-DF (32^3), LES-SDF 1 (64^3), LES-SDF 2 (128^3) and LES-SDF 3 (256^3) [see legend in panel (a) for line types]. The LES grid resolution is equal to $16\ell_k$.

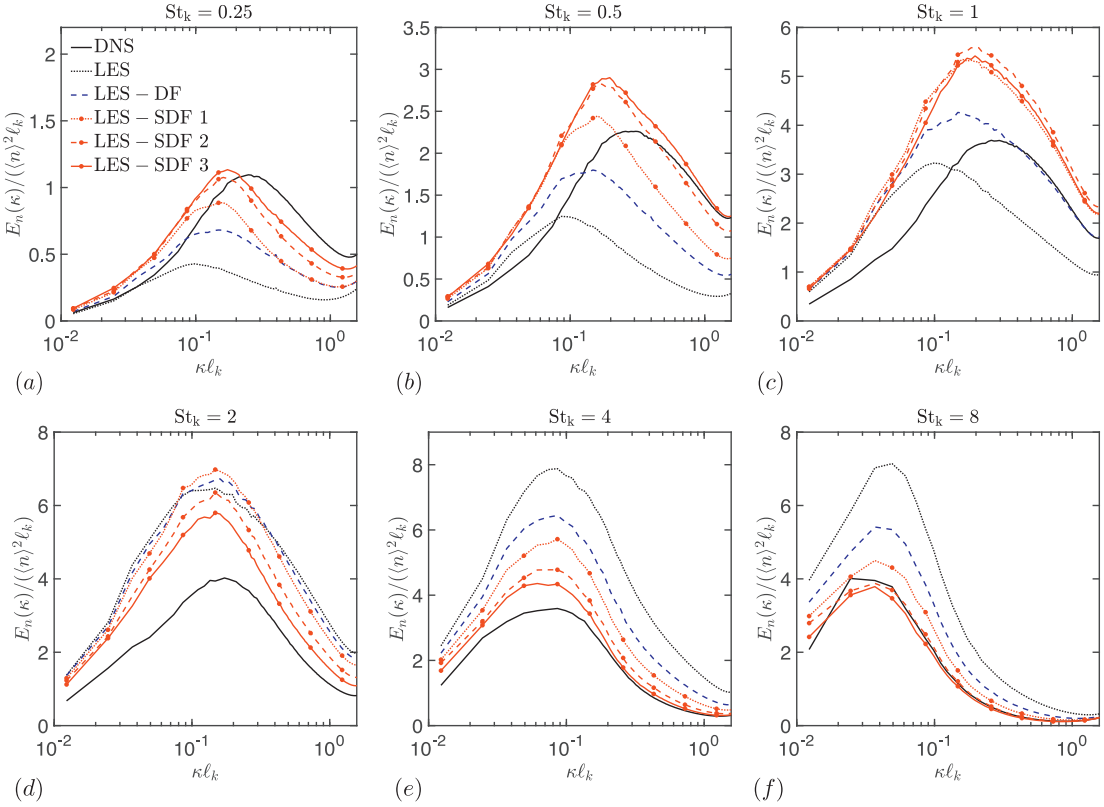

Fig. 6. Ensemble-averaged number-density Fourier spectra for (a) $\mathrm{St_k} = 0.25$, (b) $\mathrm{St_k} = 0.5$, (c) $\mathrm{St_k} = 1$, (d) $\mathrm{St_k} = 2$, (e) $\mathrm{St_k} = 4$, and (f) $\mathrm{St_k} = 8$. The different curves correspond to DNS (256^3), LES (32^3), LES-DF (32^3), LES-SDF 1 (64^3), LES-SDF 2 (128^3) and LES-SDF 3 (256^3) [see legend in panel (a) for line types]. The LES wavenumber cutoff is located at $\kappa\ell_k = 0.2$.

predictions are obtained using the SDF model with two reconstruction levels.

Note that the curve corresponding to the third reconstruction level (LES-SDF 3) overpredicts the tails of the PDF of Q. This observation, along with the overprediction of the spectra in Fig. 4(a,b), indicate that a viscous subrange would need to be introduced in the model SDF model in order to avoid such excessive deployment of energy in the third reconstruction level.

3.3. Dispersed-phase statistics

This section focuses on the performance of the SDF models described in Section 2 in predicting the intensity and scales associated with preferential concentration. For this purpose, two-point statistics are analyzed and interpreted below that consist of the radial distribution function (RDF), which quantifies the likelihood that a given pair of particles is separated by a certain radial distance (e.g., see Ray and Collins, 2011 for further details), and the energy spectrum of the particle number-density fluctuations, which characterizes the energy of the fluctuations per wavenumber.

The comparisons between RDF's obtained from DNS and LES in Fig. 5 show that the baseline LES heavily underpredicts particle clustering when the Stokes number is smaller than unity, while an equally large overprediction occurs in the opposite limit of large Stokes numbers. This observation is consistent with results obtained from a-priori filtered-DNS studies of the effect of small scales on particles motion, highlighting the opposite physical mechanisms by which small-scale fluctuations disperse or anti-disperse the particles (Minier, 2015; Ray and Collins, 2011). This poses a challenge for SGS models attempting to predict preferential concentration, in that they should be able to counteract the LES mismatches by steering the particles in a fundamentally different way on each side of the approach to the $\mathrm{St}_k \sim 1$ limit. Specifically, at small Stokes numbers, the SGS-modeled velocity should cluster or anti-disperse the particles. Conversely, at large Stokes numbers, the SGS-modeled velocity should disperse the particles.

Remarkably, the SDF model proposed here reproduces both the anti-dispersion and dispersion trends required for $\mathrm{St}_k < 1$ and $\mathrm{St}_k > 1$ regimes, respectively, and it greatly improves the predictions of the earlier differential-filter approximate-deconvolution model proposed in Park et al. (2017, 2015). An increasing agreement between the SDF model and the DNS is observed as the number of reconstruction levels increases from one to three, with exception of the unity Stokes-number case, in which an increase in the reconstruction level has no effect on the solution. On the contrary, the utilization of the SDF model at $\mathrm{St}_k \sim 1$ worsens the predictions, whereas the differential-filter approximate-deconvolution model reproduces well the RDF in DNS, yet the scales associated with the predicted particle clouds are erroneous, as described in Park et al. (2015). As the Stokes number becomes increasingly large, diminishing returns are obtained by deploying additional levels of reconstruction in SDF model, since the particles become increasingly inertial with respect to the subgrid scales (Urzay et al., 2014).

In order to address the performance of the SDF model in predicting the scales and fluctuation intensity associated with the particle concentration field, Fig. 6 shows the energy spectra of the particle number-density fluctuations E_n. Physical interpretations of the variations of this metric with the Stokes number are provided

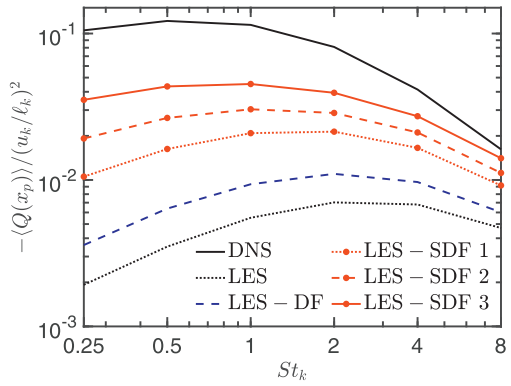

Fig. 7. Ensemble-averaged mean of the second invariant of the carrier-phase velocity-gradient tensor Q sampled by the particles as a function of the Stokes number. The different curves correspond to DNS (256^3), LES (32^3), LES-DF (32^3), LES-SDF 1 (64^3), LES-SDF 2 (128^3) and LES-SDF 3 (256^3).

elsewhere (Park et al., 2017; Jin et al., 2010). It suffices to mention here that the spectra peak occurs in the subgrid scales at $\mathrm{St}_k \leq 1$. As a result, and in the absence of appropriate spectral support, the baseline LES results lead to significant disagreements with DNS in predicting E_n. This discrepancy is manifested as artificially larger particle clouds in LES relative to those observed in DNS. On the other hand, the spectra peak occurs at resolved wavenumbers at $\mathrm{St}_k > 1$, but the maximum value of E_n is erroneous. In the LES, this renders artificially elongated clouds where the particles accumulate with an unrealistic intensity.

Significant improvements in the prediction of E_n are observed when the SDF model is employed. For instance, at $\mathrm{St}_k < 1$, both LES and the differential-filter approximate-deconvolution model miscalculate the location of the spectrum peak, which is artificially shifted toward larger scales as a result of the inaccessibility of LES to subgrid wavenumbers. In contrast, the SDF model improves the prediction of the spectra at scales smaller than the original LES grid while capturing increasingly more accurately the shift in the peak location and the peak magnitude as the level of reconstruction is increased, as shown for instance in Fig. 6(a). At $\mathrm{St}_k > 1$, the SDF model also improves the prediction of the spectrum peak and decreases the level of preferential concentration while maintaining the correct scales of the particle clouds.

Joint statistics corresponding to the mean values of Q sampled by the particles are provided in Fig. 7. Whereas the spatial mean of Q vanishes because of the flow incompressibility, the mean value of Q sampled by the particles attains negative values because of the tendency of the particles to accumulate in straining regions. As shown in Fig. 7, the SDF model improves the predictions of this quantity over the entire range of Stokes numbers tested here. This suggests that the regenerated values of Q observed in Fig. 4 lead to subgrid-scale flows that interact with particles in a reasonable manner.

These considerations are ratified by visualizing the spatial distribution of particles in Figs. 8 and 9. Specifically, the visualizations suggest that, as the number of reconstruction level is increased, the SDF model increasingly improves the performance with respect to the baseline LES and to the earlier differential-filter approximate-deconvolution model proposed in Park et al. (2017, 2015). The associated benefits are better predictions of the overall structure of the preferentially concentrated clouds of particles and their associated spatial scales. However, despite these improvements, the prediction of the range of near-unity Stokes numbers continues to be a unsolved challenge that is worthy of future work.

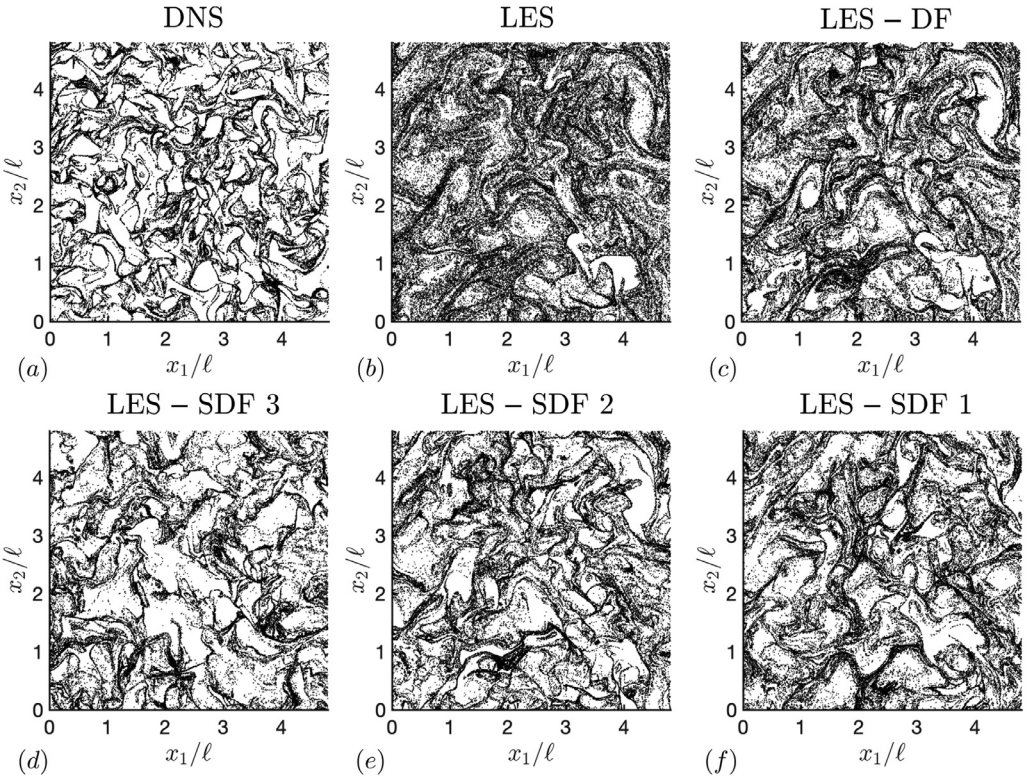

Fig. 8. Instantaneous spatial distribution of particles (dots) within a slice of thickness ℓ_k for $\mathrm{St}_k = 0.5$ for (a) DNS (256^3), (b) LES (32^3), (c) LES-DF (32^3), (d) LES-SDF 3 (256^3), (e) LES-SDF 2 (128^3), and (f) LES-SDF 1 (64^3). The LES grid resolution is 0.15ℓ.

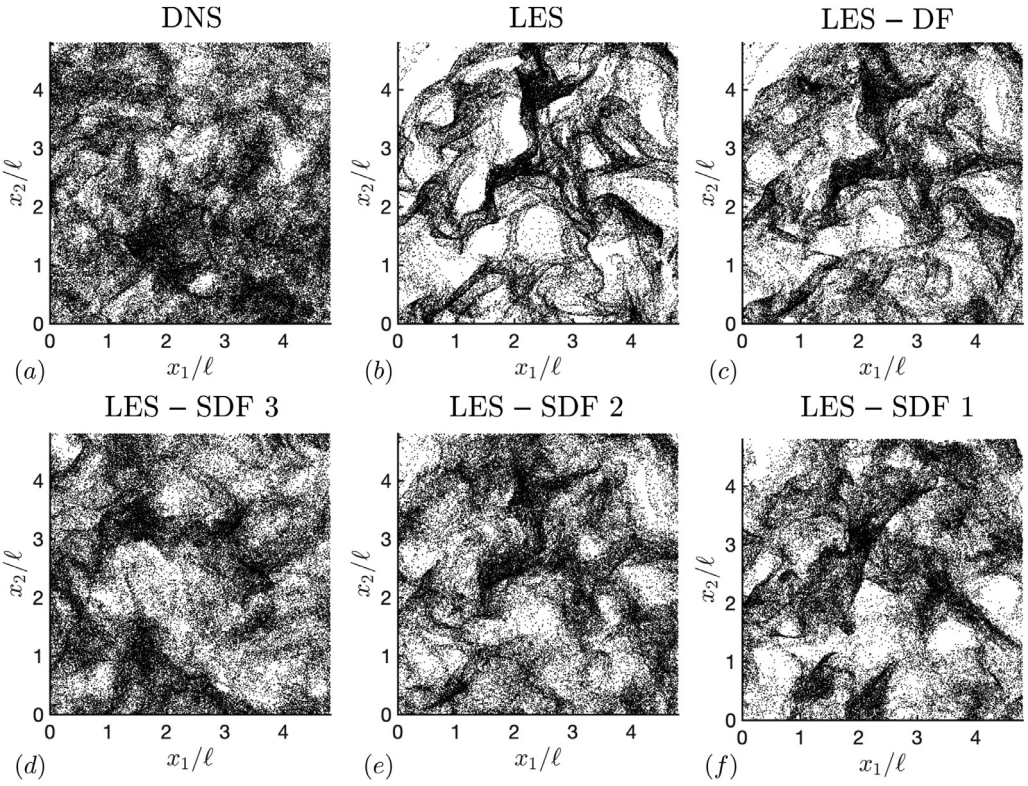

Fig. 9. Instantaneous spatial distribution of particles (dots) within a slice of thickness ℓ_k for $\mathrm{St}_k = 8$ for (a) DNS (256^3), (b) LES (32^3), (c) LES-DF (32^3), (d) LES-SDF 3 (256^3), (e) LES-SDF 2 (128^3), and (f) LES-SDF 1 (64^3). The LES grid resolution is 0.15ℓ.

4. Conclusions

In this study, an SGS model for LES of particle-laden turbulence formulated in physical space is proposed, which constructs a spectrally enriched velocity field on a grid finer than the original LES grid without requiring to solve the Navier–Stokes equations on that fine grid. The model extends the dynamic differential-filter approximate-deconvolution model in Park et al. (2017, 2015) by using a dynamic reformulation of the spectrally-enriched velocity-estimation model proposed in Domaradzki and Loh (1999). The regeneration of small scales in the present model is based on non-linear, convective interactions between resolved eddies. The performance of the proposed model is assessed in homogeneous-isotropic turbulence laden with a dilute suspension of inertial point particles. In most cases, the prediction of preferential concentration is improved relative to LES without any model for the SGS velocity, and to the differential-filter approximate-deconvolution model proposed in Park et al. (2017, 2015).

In the present work, the modeled SGS velocity is solely used for integrating the particle equation of motion (3). The utilization of the SDF-modeled velocity with the objective of computing the unclosed SGS stress in Eq. (2) is worth investigating. Similarly, the utilization of the present model locally on a cell-by-cell basis, by reconstructing a spectrally enriched velocity field in physical space only in spatial regions characterized, for instance, by high concentration of particles, is also an interesting endeavor for reducing the computational cost (Bassenne et al., 2017b). In complex geometries, where the grid may no longer be Cartesian, and consequently, its elements may not be cubes or rectangular cuboids, the straightforward grid-refinement process followed in this study becomes inappropriate and requires modification. Lastly, it would be of some interest to study the applicability of this model beyond problems related to particle-laden turbulence. An example of recent work that has employed this model includes, for instance, the corrugation and breakup of liquid-gas interfaces due to unresolved turbulent velocity fluctuations (Herrmann et al., 2018).

Acknowledgements

This investigation was funded by the Advanced Simulation and Computing (ASC) program of the US Department of Energy's National Nuclear Security Administration via the PSAAP-II Center at Stanford, Grant #DE-NA0002373. The first author is grateful to Los Alamos National Laboratory for the hospitality during his stay in Summer 2017 as part of the PSAAP-II Student Visiting Program.

References

Akinlabi, E.O., Wacławczyk, M., Malinowski, S.P., 2018. Fractal reconstruction of sub-grid scales for large eddy simulation of atmospheric turbulence. J. Phys. Conf. Ser. 1101 (1), 012001.
Baker, L., Frankel, A., Mani, A., Coletti, F., 2017. Coherent clusters of inertial particles in homogeneous turbulence. J. Fluid Mech. 833, 364–398.
Balachandar, S., Eaton, J.K., 2010. Turbulent dispersed multiphase flow. Annu. Rev. Fluid Mech. 42, 111–133.
Balachandar, S., Liu, K., Lakhote, M., 2019. Self-induced velocity correction for improved drag estimation in Euler–Lagrange point-particle simulations. J. Comp. Phys. 376 (1), 160–185.
Bassenne, M., Esmaily, M., Livescu, D., Moin, P., Urzay, J., 2017a. Dynamic spectrally-enriched LES subgrid-scale modeling for preferential concentration of inertial particles in turbulence. In: Annual Research Briefs, Center for Turbulence Research. Stanford University, pp. 3–19.
Bassenne, M., Johnson, P.L., Moin, P., Urzay, J., 2018a. On wall modeling for LES of particle-laden turbulent channel flows. In: Annual Research Briefs, Center for Turbulence Research. Stanford University, pp. 93–109.
Bassenne, M., Moin, P., Urzay, J., 2018b. Wavelet multiresolution analysis of particle-laden turbulence. Phys. Rev. Fluids 3 (8), 084304.
Bassenne, M., Urzay, J., Moin, P., 2015. Spatially-localized wavelet-based spectral analysis of preferential concentration in particle-laden turbulence. In: Annual Research Briefs, Center for Turbulence Research. Stanford University, pp. 3–16.
Bassenne, M., Urzay, J., Moin, P., 2017b. Extraction of coherent clusters and grid adaptation in particle-laden turbulence using wavelet filters. Phys. Rev. Fluids 2, 054301.

Bassenne, M., Urzay, J., Park, G.I., Moin, P., 2016. Constant-energetics physical-space forcing methods for improved convergence to homogeneous-isotropic turbulence with application to particle-laden flows. Phys. Fluids 28 (3), 035114.
Bragg, A.D., Ireland, P.J., Collins, L.R., 2015. Mechanisms for the clustering of inertial particles in the inertial range of isotropic turbulence. Phys. Rev. E 92 (2), 023029.
Bürger, K., Treib, M., Westermann, R., Werner, S., Lalescu, C. C., Szalay, A., Meneveau, C., Eyink, G. L., 2013. Vortices within vortices: hierarchical nature of vortex tubes in turbulence. ArXiv:1210.3325v2.
Chen, J., Jin, G., 2017. Large-eddy simulation of turbulent preferential concentration and collision of bidisperse heavy particles in isotropic turbulence. Powder Technol. 314, 281–290.
Chen, L., Goto, S., Vassilicos, J.C., 2006. Turbulent clustering of stagnation points and inertial particles. J. Fluid Mech. 553, 143–154.
Coleman, S.W., Vassilicos, J.C., 2009. A unified sweep-stick mechanism to explain particle clustering in two-and three-dimensional homogeneous, isotropic turbulence. Phys. Fluids 21 (11), 113301.
Domaradzki, J.A., Loh, K., 1999. The subgrid-scale estimation model in the physical space representation. Phys. Fluids 11 (8), 2330–2342.
Esmaily, M., Jofre, L., Mani, A., Iaccarino, G., 2018. A scalable geometric multigrid method for nonsymmetric elliptic systems with applications to variable-density flows. J. Comp. Phys. 357, 142–158.
Esmaily-Moghadam, M., Mani, A., 2016. Analysis of the clustering of inertial particles in turbulent flows. Phys. Rev. Fluids 1 (8), 084202.
Ferrante, A., Elghobashi, S., 2003. On the physical mechanisms of two-way coupling in particle-laden isotropic turbulence. Phys. Fluids 15 (2), 315–329. doi:10.1063/1.1532731.
Frankel, A., Pouransari, H., Coletti, F., Mani, A., 2016. Settling of heated particles in homogeneous turbulence. J. Fluid Mech. 792, 869–893.
Germano, M., Piomelli, U., Moin, P., Cabot, W., 1991. A dynamic subgrid-scale eddy viscosity model. Phys. Fluids A 3 (7), 1760–1765.
Ghate, A.S., Lele, S.K., 2017. Subfilter-scale enrichment of planetary boundary layer large eddy simulation using discrete Fourier-Gabor modes. J. Fluid Mech. 819, 494–539.
Gobert, C., Manhart, M., 2011. Subgrid modelling for particle-LES by spectrally optimised interpolation (soi). J. Comput. Phys. 230 (21), 7796–7820.
Goto, S., Vassilicos, J.C., 2006. Self-similar clustering of inertial particles and zero-acceleration points in fully developed two-dimensional turbulence. Phys. Fluids 18 (11), 115103.
Goto, S., Vassilicos, J.C., 2008. Sweep-stick mechanism of heavy particle clustering in fluid turbulence. Phys. Rev. Lett. 100 (5), 054503.
He, G., Jin, G., Yang, Y., 2017. Space-time correlations and dynamic coupling in turbulent flows. Annu. Rev. Fluid Mech. 49, 51–70.
Herrmann, M., Kedelty, D., Ziegenhein, T., 2018. A dual-scale subgrid closure for LES of phase interfaces in turbulent flows. In: Proceedings of the Summer Program, Center for Turbulence Research. Stanford University, pp. 45–54.
Horwitz, J.A.K., Mani, A., 2018. Correction scheme for point-particle models applied to a nonlinear drag law in simulations of particle-fluid interaction. Int. J. Multiphase Flow 101, 74–84.
Jiménez, J., Wray, A.A., Saffman, P.G., Rogallo, R.S., 1993. The structure of intense vorticity in isotropic turbulence. J. Fluid Mech. 255, 65–90.
Jin, G., He, G.W., Wang, L.P., 2010. Large-eddy simulation of turbulent collision of heavy particles in isotropic turbulence. Phys. Fluids 22 (5), 055106.
Jofre, L., Geraci, G., Fairbanks, H., Doostan, A., Iaccarino, G., 2017. Multi-fidelity uncertainty quantification of irradiated particle-laden turbulence. In: Annual Research Briefs, Center for Turbulence Research. Stanford University, pp. 21–34.
Johnson, P., Meneveau, C., 2018. Predicting viscous-range velocity gradient dynamics in large-eddy simulations of turbulence. J. Fluid Mech. 837, 80–114.
Lazaro, B.J., Lasheras, J.C., 1989. Particle dispersion in a turbulent, plane, free shear layer. Phys. Fluids A 1 (6), 1035–1044.
Lilly, D.K., 1992. A proposed modification of the germano subgrid-scale closure method. Phys. Fluids A 4 (3), 633–635.
Marchioli, C., 2017. Large-eddy simulation of turbulent dispersed flows: a review of modelling approaches. Acta Mech. 228 (3), 741–771.
Marchioli, C., Salvetti, M., Soldati, A., 2008a. Some issues concerning large-eddy simulation of inertial particle dispersion in turbulent bounded flows. Phys. Fluids 20 (4), 040603.
Marchioli, C., Salvetti, M.V., Soldati, A., 2008b. Appraisal of energy recovering sub-grid scale models for large-eddy simulation of turbulent dispersed flows. Acta Mech. 201 (1–4), 277–296.
Maxey, M.R., 1987. The gravitational settling of aerosol particles in homogeneous turbulence and random flow fields. J. Fluid Mech. 174, 441–465.
Maxey, M.R., Riley, J.J., 1983. Equation of motion for a small rigid sphere in a nonuniform flow. Phys. Fluids 26 (4), 883–889.
Mazzitelli, I.M., Toschi, F., Lanotte, A.S., 2014. An accurate and efficient lagrangian sub-grid model. Phys. Fluids 26 (9), 095101.
Michalek, W.R., Kuerten, J.G.M., Zeegers, J.C.H., Liew, R., Pozorski, J., Geurts, B.J., 2013. A hybrid stochastic-deconvolution model for large-eddy simulation of particle-laden flow. Phys. Fluids 25, 123302.
Minier, J., 2015. On lagrangian stochastic methods for turbulent polydisperse two-phase reactive flows. Prog. Energy Combust. Sci. 50, 1–62.
Monchaux, R., Bourgoin, M., Cartellier, A., 2010. Preferential concentration of heavy particles: aVoronoï analysis. Phys. Fluids 22 (10), 103304.
Monchaux, R., Bourgoin, M., Cartellier, A., 2012. Analyzing preferential concentration and clustering of inertial particles in turbulence. Int. J. Multiphase Flow 40, 1–18.
Murray, S., Lightstone, M., Tullis, S., 2016. Single-particle lagrangian and structure statistics in kinematically simulated particle-laden turbulent flows. Phys. Fluids 28 (3), 033302.
Park, G.I., Bassenne, M., Urzay, J., Moin, P., 2017. A simple dynamic subgrid-scale model for LES of particle-laden turbulence. Phys. Rev. Fluids 2 (4), 044301.
Park, G.I., Urzay, J., Bassenne, M., Moin, P., 2015. A dynamic subgrid-scale model based on differential filters for LES of particle-laden turbulent flows. In: Annual Research Briefs, Center for Turbulence Research. Stanford University, pp. 17–26.
Pouransari, H., Mani, A., 2017. Effects of preferential concentration on heat transfer in particle-based solar receivers. J. Sol. Energy Eng. 139 (2), 021008.
Pouransari, H., Mani, A., 2018. Particle-to-fluid heat transfer in particle-laden turbulence. Phys. Rev. Fluids 3 (7), 074304.
Pozorski, J., Apte, S., 2009. Filtered particle tracking in isotropic turbulence and stochastic modeling of subgrid-scale dispersion. Int. J. Multiphase Flow 35 (2), 118–128.
Pozorski, J., Rosa, B., 2019. The motion of settling particles in isotropic turbulence: filtering impact and kinematic simulations as subfilter model. In: Direct and Large-Eddy Simulation XI. Springer, pp. 215–220.
Rahmani, M., Geraci, G., Iaccarino, G., Mani, A., 2015. Polydisperse particles in an irradiated turbulent gas-particle mixture. In: Annual Research Briefs, Center for Turbulence Research. Stanford University, pp. 27–41.
Rani, S.L., Dhariwal, R., Koch, D.L., 2014. A stochastic model for the relative motion of high stokes number particles in isotropic turbulence. J. Fluid Mech. 756, 870–902.
Ray, B., Collins, L., 2011. Preferential concentration and relative velocity statistics of inertial particles in Navier–Stokes turbulence with and without filtering. J. Fluid Mech. 680, 488–510.
Ray, B., Collins, L., 2014. A subgrid model for clustering of high-inertia particles in large-eddy simulations of turbulence. J. Turbul. 15 (6), 366–385.
Renzo, M.D., Urzay, J., 2018. Aerodynamic generation of electric fields in turbulence laden with charged inertial particles. Nat. Commun. 9.
Richter, D.H., Garcia, O., Astephen, C., 2016. Particle stresses in dilute, polydisperse, two-way coupled turbulent flows. Phys. Rev. E 93 (1), 013111.
Robinson, A., 1956. On the motion of small particles in a potential field of flow. Comm. Pure Appl. Math 9 (1), 69–84.
Schiavazzi, D., Coletti, F., Iaccarino, G., Eaton, J.K., 2014. A matching pursuit approach to solenoidal filtering of three-dimensional velocity measurements. J. Comp. Phys. 263, 206–221.
Shotorban, B., Mashayek, F., 2006. A stochastic model for particle motion in large-eddy simulation. J. Turbul. 7, N18.
Squires, K.D., Eaton, J.K., 1991. Preferential concentration of particles by turbulence. Phys. Fluids 3 (5), 1169–1178.
Urzay, J., Bassenne, M., Park, G.I., Moin, P., 2014. Characteristic regimes of subgrid-scale coupling in LES of particle-laden turbulent flows. In: Annual Research Briefs, Center for Turbulence Research. Stanford University, pp. 3–13.
Villafañe, L., Banko, A., Elkins, C., Eaton, J.K., 2017. Gas heating by radiation absorbing inertial particles in a turbulent duct flow. In: Annual Research Briefs, Center for Turbulence Research. Stanford University, pp. 35–47.
Wang, L.P., Maxey, M.R., 1993. Settling velocity and concentration distribution of heavy particles in homogeneous isotropic turbulence. J. Fluid Mech. 256, 27–68.
Yao, Y., Capecelatro, J., 2018. Competition between drag and coulomb interactions in turbulent particle-laden flows using a coupled-fluid–Ewald-summation based approach. Phys. Rev. Fluids 3 (3), 034301.
Zhou, Z., Wang, S., Jin, G., 2018. A structural subgrid-scale model for relative dispersion in large-eddy simulation of isotropic turbulent flows by coupling kinematic simulation with approximate deconvolution method. Phys. Fluids 30 (10), 105110.